N-doped Fe@CNT for combined RWGS/FT CO_2 hydrogenation

David L. Williamson[†], Carmelo Herdes[†], Laura Torrente-Murciano[‡], Matthew D. Jones[,§] and Davide Mattia[*,†]*

[†] Department of Chemical Engineering, University of Bath

Claverton Down, Bath BA2 7AY, UK

[‡] Department of Chemical Engineering and Biotechnology

University of Cambridge, West Cambridge Site,

Philippa Fawcett Drive, Cambridge CB3 0AS, UK

[§] Department of Chemistry, University of Bath

Claverton Down, Bath BA2 7AY, UK

Corresponding Authors

* Dr. Matthew D. Jones, E-mail: m.jones2@bath.ac.uk, Telephone: +44 (0) 1225 384908.

* Professor Davide Mattia, E-mail: d.mattia@bath.ac.uk, Telephone: +44 (0) 1225 383961.

ABSTRACT: Conversion of CO_2 into chemical fuels represents an attractive route for green house gas (GHG) emissions reductions and renewable energy storage. Iron nanoparticles supported on graphitic carbon materials (e.g. carbon nanotubes) have proven themselves to be effective catalysts

for this process. This is due to their stability and ability to support simultaneous reverse water gas shift and Fischer-Tropsch catalysis. Typically, these catalytic iron particles are post-doped onto an existing carbon support via wet impregnation. Nitrogen doping of the catalyst support enhances particle-support interactions by providing electron-rich anchoring sites for nanoparticles during wet impregnation. This is typically credited for improving CO_2 conversion and product selectivity in subsequent catalysis. However, the mechanism for RWGS/FT catalysis remains underexplored. Current research places significant emphasis on the importance of enhanced particle-support interactions due to N-doping, which may mask further mechanistic effects arising from the presence or absence of nitrogen during CO_2 hydrogenation. Here we report a clear relationship between the presence of nitrogen in the CNT support of a RWGS/FT iron catalyst, and significant shifts in the activity and product distribution of the reaction. Particle-support interactions are maximized (and discrepancies between N-doped and pristine support materials minimized) by incorporating iron and nitrogen directly into the support during synthesis. Reactivity is thus rationalized in terms of the influence of C—N dipoles in the support upon the adsorption properties of CO_2 and CO on the surface, rather than improved particle-support interactions. These results show that the direct hydrogenation of CO_2 to hydrocarbons is a potentially viable route to reduce carbon emissions from human activities.

KEYWORDS: CO_2, catalysis, nitrogen, doping, iron, carbon nanotube, hydrocarbon, water gas shift, Fischer-Tropsch, storage, adsorption, simulation

INTRODUCTION:

The water gas shift (WGS) [1] and Fischer-Tropsch (FT) [2] processes have long been used in industry for hydrogen and hydrocarbon formation.[1-8]

$$CO + H_2O \rightleftharpoons CO_2 + H_2 \quad [1]$$

$$(2n+1)H_2 + nCO \rightarrow C_nH_{2n+2} + nH_2O \quad [2]$$

However, to mitigate CO_2 emissions and cope with the intermittent supply patterns of renewable energy sources, research has been increasingly focused on converting CO_2 into hydrocarbon fuels. This could allow for energy storage directly from CO_2 and excess renewable energy.[9-14] Coupling the reverse water gas shift (RWGS) and FT reactions together into a single process is considered to be especially desirable.[15] Simultaneous consumption of CO produced by RWGS via subsequent FT catalysis shifts the equilibrium of the RWGS reaction towards products, enhancing the overall efficiency of the process.[16-17]

Iron-based catalysts are particularly amenable to this process, as the high temperature RWGS reaction is catalyzed by promoted iron oxides,[1, 18-20] and the Hägg carbide is active in FT catalysis.[11, 21-25] Iron nanoparticles supported on carbon nanotubes (often referred to as Fe-CNT or Fe/CNT type catalysts) have proven themselves to be active catalysts for this coupled process due to their stability, adsorption capacity, and ability to support the active species of both reactions.[26-27] It has also been shown that increasing interactions between the catalytic nanoparticles and the CNT support is critical to achieve high activity in Fe/CNT catalysts. Catalysts where the iron particles have been integrated into the CNT support directly during synthesis (Fe@CNT) are significantly more active than catalysts where particles have been doped onto the CNT support in a separate step.[15, 26, 28-35]

Functionalisation of the CNT support has been explored in recent years as a means of enhancing these particle-support interactions.[11, 36-37] Nitrogen incorporation leads to improved conversion, reducibility and particle dispersion, which has been attributed to increased overlap between the metal 3d orbitals and excess π-electron density in the graphitic plane.[11, 36, 38-40] However, studies

until this point have focused exclusively on the effect of nitrogen doping in pure FT synthesis, or have only investigated catalysts where the nitrogen and iron nanoparticles have been post-doped onto an existing CNT support separately.[11, 36] This limits interactions between the three key components of the catalyst, and makes it difficult to draw conclusions regarding the isolated mechanistic effects arising from the presence or absence of nitrogen in the support during CO_2 hydrogenation. In these instances, nitrogen doping is certain to affect the intrinsic activity of the catalyst significantly by influencing particle dispersion on the support, and the magnitude of support-particle interactions once the particles are deposited.[11, 36, 39, 41]

In this work we aim to elucidate the influence of nitrogen doping of graphitic carbon nanotube supports for CO_2 conversion catalysis by enhancing the magnitude of (and reducing the discrepancy between) particle-support interactions in Fe/CNT- and Fe/NCNT-type catalysts. Here we report the clearest comparison yet between the reactivity of cohesive Fe@CNT and Fe@NCNT in combined RWGS/FT catalysis for CO_2 hydrogenation, where iron and nitrogen have both been incorporated into the catalyst directly during CVD synthesis. This provides the most thorough possible integration between all elements of the catalyst and offers insights into the effect of nitrogen doping on the overall CO_2 hydrogenation process through combined characterization, catalytic testing and molecular dynamics simulations.

EXPERIMENTAL:

Catalyst synthesis was achieved as follows: To produce Fe@CNT, 1.0 g ferrocene (FcH) was dissolved in 50 mL toluene to produce a CVD precursor solution of concentration 20 mg mL-1 FcH in toluene. 40 mL of the precursor solution was then injected at a rate of 10 mL h^{-1} into a quartz tube (25 mm ID x 28 mm OD x 122 cm L), loaded in a tubular furnace at 790 °C under a flow of 50 sccm H_2 and 400 sccm Ar. After 4 hours of CVD injection, the raw catalyst was readily

retrieved from within the quartz tube by scratching the interior cavity of the quartz tube with an elongated spatula. A 40 mL injection synthesis typically yielded ca. 1.5 g of catalyst. To produce Fe@NCNT, the same procedure was employed while replacing toluene in the precursor solution with acetonitrile (ACN) to act as a source of both carbon and nitrogen during the CNT growth process. To minimize error due to variance between catalyst batches, a stock of ca. 10 g was produced before beginning catalytic trials, and topped up every 3 reactions. 0.5 wt. % Na doping was achieved in Na-Fe@NCNT via wet impregnation. 9 mg NaHCO3 (Sigma-Aldrich, 99.7%) was dissolved in 15 mL deionized water with 0.5 g Fe@NCNT. The slurry was stirred for 24 hours and subsequently heated at 115 °C for 2 hours before collecting the dried powder.

Catalysts activation was achieved by loading 0.47 g of the into a stainless steel calcination tube (0.5 inch OD x 0.451 ID x 6 inch L). This tube was plugged at one end with quartz wool (9-30 micron, H. Baumbach & Co Ltd) to prevent the catalyst from escaping while still allowing for air flow. For Fe@ NCNT-based materials, the tube was then heated in a muffle oven at 400 °C for 1 hour under a static air atmosphere, with a heating ramp rate of 10 °C min^{-1}. For any Fe@CNT-based materials, the same process was repeated, though the catalysts were instead heated to 570 °C for 40 min. Further information on the origin of these different activation temperatures can be found in the ESI.

CO_2 conversion testing was conducted by loading 0.4 g of the desired catalyst into a stainless steel reaction tube (0.5 inch OD x 0.451 inch ID x 6 inch L), which was plugged with quartz wool (9-30 micron, H. Baumbach & Co Ltd) at both ends to ensure that the catalyst powder rested securely in the middle of the tube. The sample was then placed in a tubular furnace and heated to 400 °C for 3 hours under a flow of 50 sccm H_2 to reduce the catalyst. To begin the combined RWGS/FT process, the temperature was lowered to 370 °C and the was pressure gradually raised

to 15 bar while maintaining the desired reaction gas ratio (3:1 H_2:CO_2). A high overall flow rate (180 sccm) was employed during this step to facilitate pressurization of the reactor. When the desired pressure had been achieved, the flow rate was lowered to the reaction flow rate of 8 sccm. The reactor was left for 2 hours to equilibrate following pressurization, after which samples were taken hourly for 3 hours via a 50 mL SGE gas tight syringe with leur-lock fittings and analyzed via GC-MS. An Agilent Technologies 7890A GC System with Agilent Technologies 5975C insert MSD with Triple-Axis Detector (MS, TCD, FID) was used as the GC-MS instrument. The installed column was an HP-Plot Q column. The TCD was used to quantify CO_2 and CO, while the FID was used to quantify hydrocarbon species. 1% Ar in H_2 was used as the source in CO_2 conversion experiments so that Ar could be used as an internal standard during GC-MS measurements.

It should be noted that the chosen reaction conditions have been previously identified as producing noteworthy CO_2 and CO conversion over Fe@CNT-type materials.[15] However, the stated flow rate of 8 sccm should be considered low for the tested catalyst powder mass of 0.4 g. Diffusion limitations may play a role in masking the intrinsic activity of the catalyst and conditions at the catalyst surface. Further work must be conducted to optimize the reaction process.

Catalyst characterization was achieved with Raman, TEM, XPS, XRD, and TPD. Raman analysis was conducted using a Renishaw InVia system with a 532 nm laser. For CNT-based materials, a laser power of 5% was employed with the standard exposure time to facilitate quick analysis without burning or damaging the sample during analysis. For NCNT-based materials, the laser power was reduced to 0.1% due to the decrease in the stability of the CNT lattice caused by nitrogen doping leading to significant decomposition under even 1% laser power. Consequently, the exposure time for NCNT-based samples was also increased substantially to 400 seconds to

collect a clear Raman spectrum. TEM analysis was conducted using a JEOL JSM-2100PLUS at an accelerating voltage of ca. 200 kV. Particle and tube diameters were measured using the open source image processing package Fiji. XPS analysis was conducted using a Kratos Axis Ultra-DLD system. Samples were analyzed using a micro-focused monochromatic Al X-ray source (72 W) over an area of approximately 400 microns. Data was recorded at pass energies of 150 eV for survey scans and 40 eV for high resolution scan with 1 eV and 0.1 eV step sizes respectively. Charge neutralization of the sample was achieved using a combination of both low energy electrons and argon ions. XRD analysis was conducted using a Bruker D8 Advance with Vantec Detector using Cu K-α1 radiation was used to analyze all samples, which were scanned in flat plate mode from 20-80° at a scan rate of 0.27° min-1 (4 hours per sample). H_2, CO and CO_2 TPD analysis were conducted using a Micrometrics AutoChem II 2920 V4.03 Automated Catalyst Characterization System with Thermal Conductivity Detector (TCD). Samples were subjected to temperature programmed reduction up to 1000 °C at 10 °C min-1 (50 sccm 5% H_2 in Ar), pulse chemisorption of the desired analysis gas (50 sccm, 5% in He) and subsequent TPD. A detailed simulation methodology for the molecular dynamics simulations can be found in the ESI.

RESULTS AND DISCUSSION:

The Fe@CNT and Fe@NCNT catalysts were synthesized via a single-step CVD decomposition of ferrocene dissolved in toluene (for Fe@CNT) or acetonitrile (for Fe@NCNT), as previously reported.[42] Comparison of these materials using Raman, TEM, XPS and XRD reveals clear nitrogen doping in the CNT support while maintaining a similar overall morphology. Raman spectra of both samples display sharp peaks at 1354 cm^{-1} and 1597 cm^{-1} (Fig. 1), which are assigned to the D and G bands, respectively. These are typically observed in the Raman spectra of CNT-based materials.[43] The D band becomes more intense as the number of defects in the sample

increases, and so the ratio of these peaks (I_D/I_G) is often used as a measure of the overall order in a sample. Fe@CNT display a low I_D/I_G value of 0.2, while I_D/I_G for Fe@NCNT is much larger at 0.9. This increase in I_D/I_G is an indication of nitrogen incorporation in the CNT lattice, as the number of defects in the lattice increases due to poor assimilation of nitrogen atoms into the sp^2 hybridized network.[39, 43-48] The final feature at ca. 2666 cm^{-1} is the G' band, which is caused by two-phonon scattering processes that are free from the defect structures.[49-51] It is therefore suppressed in Fe@NCNT where defects are more prominent.

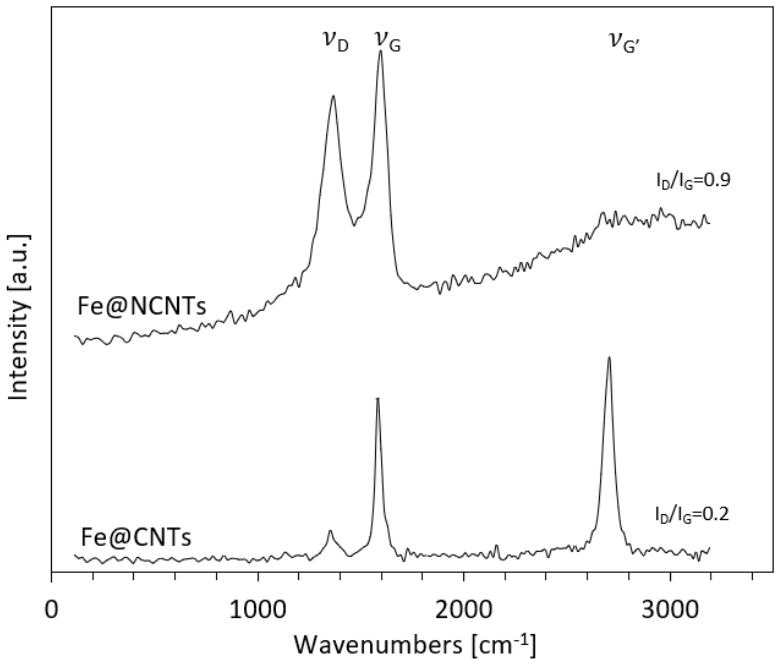

Figure 1. Raman spectra of Fe@CNTs and Fe@NCNTs after activation in air for 1 hour at 570 °C and 400 °C.

TEM analysis shows a similar morphology between the two materials, with a change in the internal bore structure attributed to the presence of nitrogen in Fe@NCNT (Fig. 2). In both cases, samples are composed of highly aligned bundles of nanotubes, with iron particles embedded into the CNT or NCNT support. In Fe@NCNT the average particle and tube diameters are 25 (±8) nm

and 35 (±21) nm, respectively, while Fe@CNT exhibit values of 34 (±11) nm and 35 (±14) nm. While these values are not identical, literature suggests that their activity and selectivity should be comparable, as particle size does not become a significant factor in FT catalysis until particle size decreases below 7 nm.[52] Fe@NCNT also display clear bamboo segmentation along the interior bore of the tubes. This is further evidence of nitrogen incorporation into the CNT lattice, as the previously discussed sp^2 defects cause the lattice to deviate from the typical hollow CNT morphology observed in Fe@CNT.[45-47]

It is currently difficult to identify the origin of this difference in particle sizes despite largely identical synthesis conditions. In conventional supported iron nanoparticle catalysts, where the iron has been doped onto the catalyst surface via wet impregnation, nitrogen doping has been observed to improve dispersion and affect particle size by providing electron-rich anchoring sites for the nucleation and stabilization of metallic nanoparticles.[11, 36, 39] However, in Fe@CNT and Fe@NCNT the addition of iron nanoparticles is governed by the CNT growth mechanism during CVD synthesis rather than the mechanism of nanoparticle nucleation during wet impregnation. Because these residual particles are typically removed as impurities during commercial CNT production processes, the mechanisms and variables governing their formation remain unexplored and explanations for their different particle sizes remains a matter of debate. It is worth noting that the observed particle sizes are within the margin of error from each other. We therefore consider them as effectively similar for the purpose of this investigation.

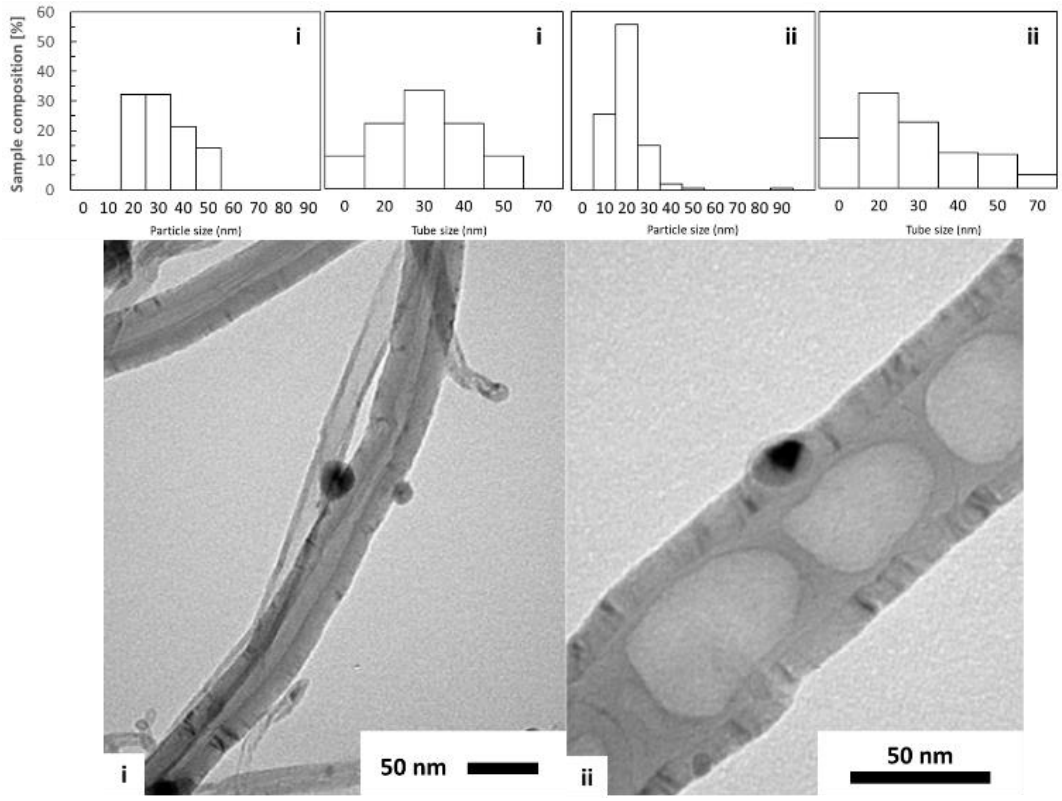

Figure 2. TEM micrographs, particle and tube size distributions of (i)Fe@CNT and (ii) Fe@NCNT after activation in air for 1 hour at 570 °C and 400 °C.

XPS spectra further confirm the presence of ca. 3 at. % nitrogen in the Fe@NCNT sample, with ca. 1 at. % iron exposed for catalysis in both Fe@CNT and Fe@NCNT after activation (SI, Table 1). Fe 2p spectra for Fe@NCNT (Fig 3.ii) suggests the formation of Fe_8N and $Fe_{16}N_2$ after synthesis, as evidenced by peaks at 707.2, 708.0, and 710.5 eV.[53] These peaks shift to 707.5, 709.9, and 711.3 eV after oxidation in air to expose the iron particles for catalysis, suggesting the formation of Fe(0), Fe(II) and Fe(III) as a mix of Fe_2O_3 and Fe_3O_4 and metallic iron, respectively.[54-55] A similar shift is observed for the iron carbides in Fe@CNT.[34] N 1s spectra for Fe@NCNT (Fig. 3.i) display peaks at ca. 398.8, 401.3, and 404.4 eV, corresponding to the presence of pyridinic, graphitic and physisorbed N_2 or chemisorbed N–O species, respectively.[39-

[40, 43, 48] These peaks initially appear at a ratio of 1:2:1 after synthesis, though this shifts to a ratio of 1:3:0 as the pyridinic, chemisorbed and physisorbed peaks are suppressed during the thermal activation process. This suggests that the nitrogen species in the CNT lattice consist primarily of graphitic nitrogen prior to catalytic testing. This may be significant, as different nitrogen environments have been noted to encourage different reactivity due to discrepancies in electron availability (e.g. graphitic nitrogen forms a shallow donor state, while the valence electrons in pyridinic and pyrrolic nitrogen sites remain confined to the π_z orbital).[36, 39, 56]

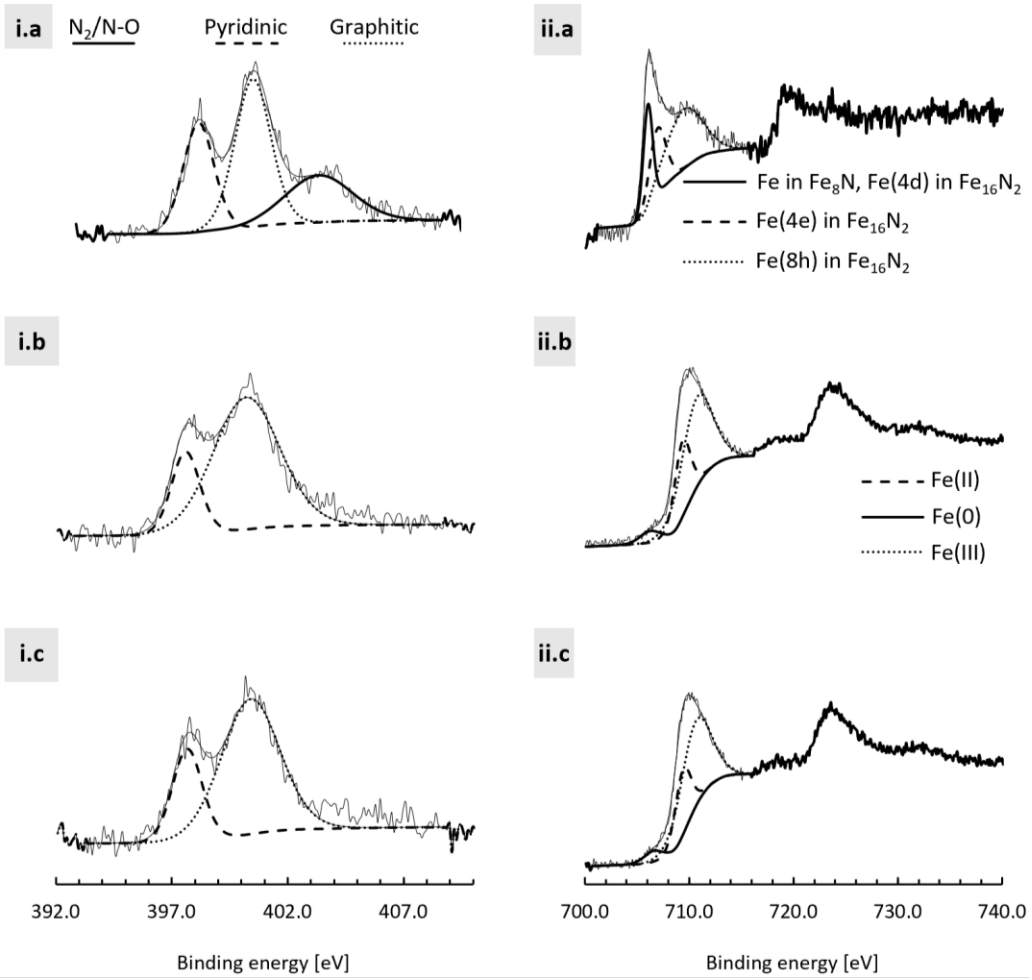

Figure 3. XPS spectra of (i) Fe@NCNT N 1s region (ii) Fe@NCNT Fe 2p region, (a) freshly synthesized, (b) activated at 400 °C in air for 1 hour, and (c) after a typical CO_2 reduction reaction.

pXRD further confirms similarities in the morphology and iron species of the two samples (Fig. 4). Both samples exhibit reflections at 26.4° corresponding to the CNT support structure. Reflections at 30.5°, 35.8°, 43.4°, 54.1°, 57.6°, and 62.5° confirm the presence of Fe_3O_4 in both samples,[57] while reflections at 24.2°, 30.4°, 33.3°, 35.8°, 41.0°, 49.6°, 54.1°, 57.6°, 62.5°, and 63.9° confirm the presence of Fe_2O_3.[58] Iron carbides are also visible as a characteristic grouping of overlapping peaks between 40° and 50°.[59] Fe@CNT appear to have more intense reflections from Fe_2O_3, which is likely an effect of the higher activation temperature (T_{act}) required to expose the iron particles for catalysis due to the greater thermal stability of the Fe@CNT (T_{act} = 570 °C) compared to Fe@NCNT (T_{act} = 400 °C).[34] Further justification of this difference in activation conditions can be found in the ESI. Beyond this difference, which is itself mitigated during catalyst reduction prior to catalysis,[26] pXRD suggests similar iron species between the iron particles of Fe@CNT and Fe@NCNT, with limited effect on the particles due to nitrogen doping. Reducing the Fe@NCNT sample results in suppression of the iron oxides and clear evolution of metallic iron characterized by reflections at 44.9° and 64.9°.[60] This is in good agreement with previous XRD studies of the Fe@CNT material.[26]

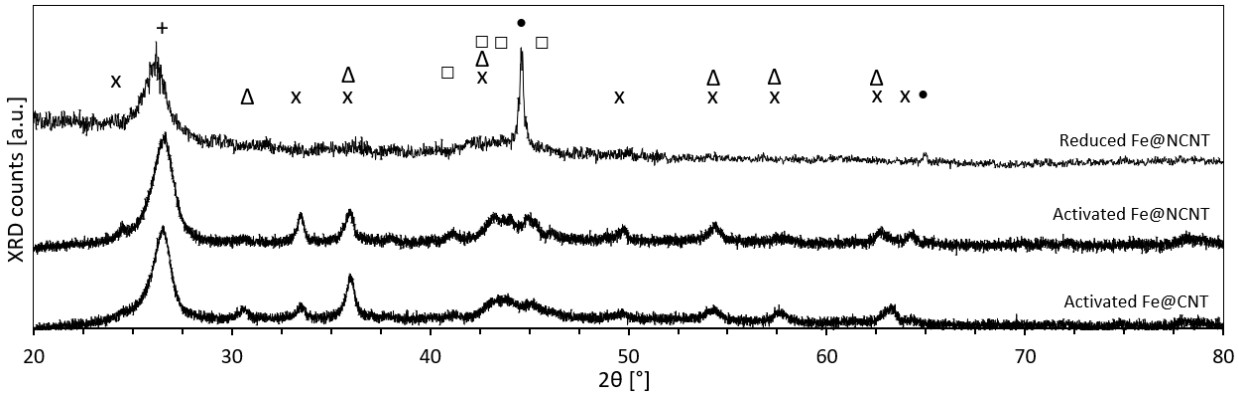

Figure 4. pXRD spectra of Fe@CNT and Fe@NCNT after activation at 400 °C (or 570 °C for Fe@CNT) in air for 1 hour. Fe@NCNT after reduction in 50 sccm H_2 at 400 °C and atmospheric

pressure are also included. Spectra indicate the presence of the CNT support (+), Fe_2O_3 (x), Fe_3O_4 (Δ), iron carbides (□), metallic iron (•).

Despite similarities in morphology and iron species, Fe@CNT and Fe@NCNT perform notably differently when applied in catalytic CO_2 hydrogenation (Fig. 5). Fe@CNT result in lower overall conversion while favoring the production of CO, olefins and $C_{n>1}$ hydrocarbons. Nitrogen doping in Fe@NCNT appears to increase conversion of CO_2 and CO significantly, simultaneously shifting selectivity towards paraffins and methane. Nitrogen doping therefore appears to play a significant role in modulating the activity and selectivity of the catalyst. The reductive character of the iron catalyst may be enhanced through electron donation from the doped nitrogen, though this would be expected to increase activity without shifting product selectivity, or even enhance FT activity with additional $C_{n>1}$ formation rather than the significant increase in methane selectivity that is observed.[39-40, 56] Catalyst-support interactions have been maximized in both materials by integrating the catalytic iron particles directly into the CNT (or NCNT) support structure, and the catalyst compositions and morphologies appear to be largely identical aside from the nitrogen content of the support material itself. This suggests that additional mechanistic influences from nitrogen doping in the catalyst support (beyond just catalyst-support interactions) are affecting the outcome of the combined RWGS/FT process.

More specifically, the increased conversion, methane selectivity, and decreased CO selectivity in Fe@NCNT suggests that nitrogen doping serves to enhance RWGS activity and initial FT conversion into methane. At the same time, further reduction of C_1 FT intermediates into longer hydrocarbons via subsequent FT polymerization is disfavored. Interestingly, this trend appears to reflect an increased affinity for dipole-containing reactants (e.g. CO, CO_2), while favoring the desorption of nonpolar products (e.g. short hydrocarbons). It is therefore possible that increased

attraction between the reactants and the catalyst increases their local concentration and serves to improve catalyst activity at the expense of long chain hydrocarbon formation. Similar effects have been reported for the enhanced adsorption of O_2 in the oxygen reduction reaction due to the presence of C–N dipoles and nitrogen environments in N-doped CNT and graphene catalysts.[39, 61-62] However, this effect has not been previously considered as a significant factor in RWGS or FT reactivity.

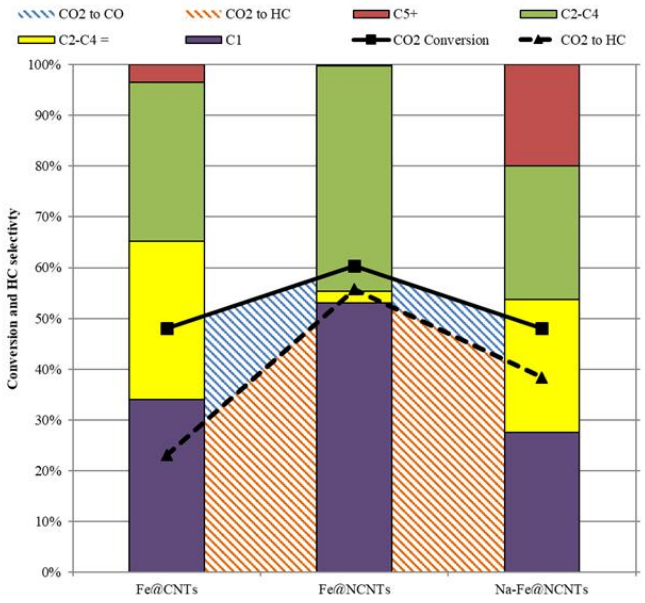

	CO_2 conversion [%]	CO selectivity [%]	HC selectivity [%]	Hydrocarbon distribution [%] CH_4	C_{2-4}	C_{5+}	Olefin/paraffin ratio
Fe@CNT	48.0	52.0	48.0	34.0	62.5	3.5	1.0
Fe@NCNT	60.3	8.6	91.4	53.0	46.6	0.3	0.1
Na-Fe@NCNT	48.0	24.8	75.2	27.5	52.5	20.0	0.5

Figure 5. Effect of nitrogen doping on combined RWGS/FT reactivity at 370 °C, 15 bar, 8 sccm and an H_2:CO_2 ratio of 3:1 using 0.4 g catalyst reduced in 50 sccm H_2 at 400 °C for 3 hours.

H_2 TPR, CO_2 and CO TPD spectra (Fig. 6.i-iii) indicate that Fe@NCNT are more easily reduced than Fe@CNT, as expected,[11] but also indicate that CO_2 and CO adsorb more strongly to the catalyst surface in Fe@NCNT. CO chemisorption has been observed to occur at ca. 400 °C over

Fe/CNT in literature.[36] Thus, peak ζ has been attributed to chemisorbed CO and peak ε has been attributed to physisorbed CO (Fig. 6.ii). While the desorption of chemisorbed CO appears largely unchanged between samples (ca. 395 °C), physisorbed CO desorbs at a notably higher temperature in Fe@NCNT. Stronger chemisorption by CO_2 at nitrogen sites is also observed in Fe@NCNT, where only physisorption is observed in Fe@CNT.[36] This increased attraction is mirrored in molecular dynamics simulations of the 3:1 H_2:CO_2 feed gas adsorption process (Fig. 6iv). Interactions between CO_2 and the catalyst surface are notably stronger in Fe@NCNT, and a slight catalytic smoothing effect can be observed in the equlibration of reactants on the catalyst (Fig. 6.v). As CO_2 and CO are dipole-containing molecules, the C–N dipoles generated in the CNT lattice through nitrogen doping are likely sources of this enhanced attraction. Furthermore, it must be noted that the hydrocarbon products of this hydrogenation do not possess such dipoles, and are therefore at a relative disadvantage in terms of attraction to the catalyst compared to new CO_2 and CO reactant molecules. This can further influence their potential for chain lengthening by encouraging termination of the FT hydrogenation process via desorption after methane formation to facilitate coordination of new CO_2 and CO reactants.

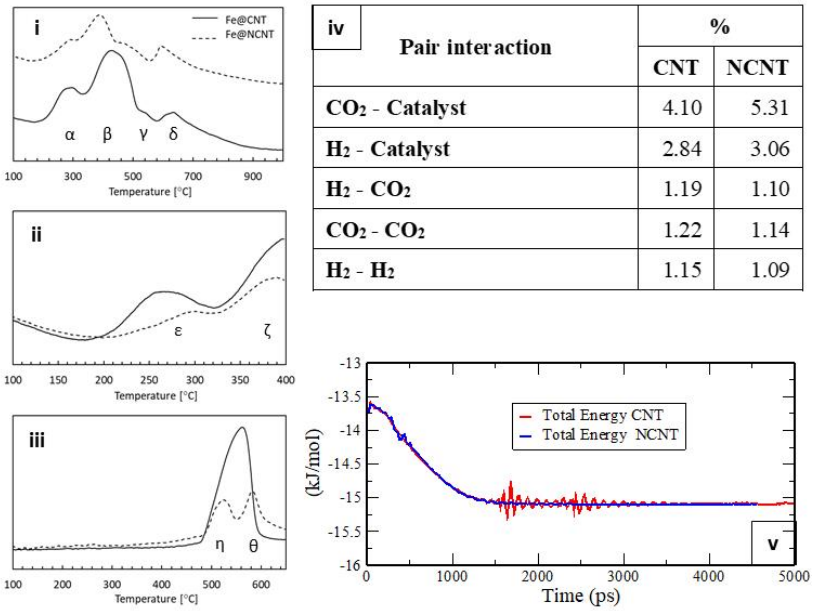

Pair interaction	%	
	CNT	NCNT
CO_2 - Catalyst	4.10	5.31
H_2 - Catalyst	2.84	3.06
H_2 - CO_2	1.19	1.10
CO_2 - CO_2	1.22	1.14
H_2 - H_2	1.15	1.09

Figure 6. (i) H_2 TPR, where α = Fe_2O_3→Fe_3O_4, β = Fe_3O_4→Fe(0), γ = Fe_3O_4→Fe(0) via FeO, and δ = gasification of the CNTs. (ii) CO TPD, where ε = physisorbed CO and ζ = chemisorbed CO. (iii) CO_2 TPD, where η = physisorbed CO_2 and θ = chemisorbed CO_2. (iv, v) simulated 3:1 H_2:CO_2 feed gas adsorption energies on Fe@CNT and Fe@NCNT. Detailed simulation methodology can be found in the ESI.

Sodium was doped onto Fe@NCNT via wet impregnation in an attempt to mask this effect by obscuring the nitrogen sites during catalysis via Na^+ coordination (Na-Fe@NCNT, Fig. 5). When

Na-Fe@NCNTs were tested in RWGS/FT catalysis, their behavior was observed to shift significantly back towards that of standard Fe@CNT, leading to reduced CO_2 and CO conversion, and increased olefin and $C_{n>1}$ hydrocarbon production. The slight increase in production of C_{5+} hydrocarbons is likely an effect of the increased basicity caused by sodium doping, as has been previously observed.[15] Additional characterization of Na-Fe@NCNT is discussed in the ESI.

This further supports the hypothesis that nitrogen doping in CNT or graphitic supports for RWGS/FT hydrogenation does not only influence the process through increased interactions between the support and its catalytic nanoparticles. Moreover, the resulting C–N dipoles in the catalyst surface also play a significant role in determining the attraction of reagants to the catalyst surface. This increased attraction appears to enhance catalyst activity by increasing the local concentration of dipole-contaning RWGS and FT reactants at the expense the formation of long-chain hydrocarbon formation. It is unclear whether the presence of different nitrogen species in the catalyst might result in a notably different outcome, though it should be noted that this effect may hold more strongly for materials in which graphitic nitrogen is most present. These findings suggest that while nitrogen doping can be a powerful tool in improving the performance of CO_2 and CO hydrogenation catalysts, it may be more preferably employed in materials intended for methanation rather than long-chain hydrocarbon production.

ASSOCIATED CONTENT

Supporting Information

Additional XPS characterization, full catalyst activation study to justify activation conditions, and detailed simulation methodology (PDF). Data created during this research are openly available from the University of Bath data archive at http://dx.doi.org/10.5125/BATH-00616

AUTHOR INFORMATION

Corresponding Authors

* Dr. Matthew D. Jones, E-mail: m.jones2@bath.ac.uk, Telephone: +44 (0) 1225 384908.

* Professor Davide Mattia, E-mail: d.mattia@bath.ac.uk, Telephone: +44 (0) 1225 383961.

Author Contributions

The manuscript was written through contributions of all authors. All authors have given approval to the final version of the manuscript.

Funding Sources

The authors would like to thank the UK Engineering and Physical Sciences Research Council (EPSRC) for their generous funding of this research.

ACKNOWLEDGMENT

The authors would like to acknowledge the following entities for their critical contributions to this work: the Microscopy and Analysis Suite (MAS) at the University of Bath for their assistance and expertise in characterizing the described materials via Raman and TEM. The Material and Chemical Characterization Facility (MC^2) at the University of Bath for their expertise in characterizing the described materials via TG-MS. Dr Gabriele Kociok-Köhn at the University of Bath Department of Chemistry for her expertise in characterizing the described materials via pXRD. The National EPSRC XPS Users' Service (NEXUS) at Newcastle University for their assistance and expertise in characterizing the underling Fe@NCNT materials via XPS.

ABBREVIATIONS

FT, Fischer-Tropsch; WGS, water gas shift; RWGS, reverse water gas shift; CNT, carbon nanotubes; TEM, transmission electron microscopy; XPS, X-ray photoelectron spectroscopy; pXRD, powder X-ray diffraction; TPD, temperature programmed desorption; CVD, chemical vapor deposition; SCCM, standard cubic centimeter; GC-MS, gas chromatography-mass spectrometry.

REFERENCES

1. Ratnasamy, C.; Wagner, J. P., Water Gas Shift Catalysis. *Catalysis Reviews* **2009,** *51* (3), 325-440, DOI 10.1080/01614940903048661.
2. Smith, R. J. B.; Loganathan, M.; Shantha Murthy, S., A Review of the Water Gas Shift Reaction Kinetics. *IJCRE* **2010,** *8* (1), R4, DOI 10.2202/1542-6580.2238.
3. Grenoble, D. C.; Estadt, M. M.; Ollis, D. F., The chemistry and catalysis of the water gas shift reaction: 1. The kinetics over supported metal catalysts. *J. Catal.* **1981,** *67* (1), 90-102, DOI 10.1016/0021-9517(81)90263-3.
4. Lin, J.; Wang, A.; Qiao, B.; Liu, X.; Yang, X.; Wang, X.; Liang, J.; Li, J.; Liu, J.; Zhang, T., Remarkable Performance of Ir1/FeOx Single-Atom Catalyst in Water Gas Shift Reaction. *J. Am. Chem. Soc.* **2013,** *135* (41), 15314-15317, DOI 10.1021/ja408574m.
5. Van Der Laan, G. P.; Beenackers, A. A. C. M., Kinetics and Selectivity of the Fischer–Tropsch Synthesis: A Literature Review. *Catalysis Reviews* **1999,** *41* (3-4), 255-318, DOI 10.1081/CR-100101170.
6. Dry, M. E., The Fischer–Tropsch process: 1950–2000. *Catal. Today* **2002,** *71* (3), 227-241, DOI 10.1016/S0920-5861(01)00453-9.
7. Dry, M. E., The Fischer-Tropsch process - commercial aspects. *Catal. Today* **1990,** *6* (3), 183-206, DOI 10.1016/0920-5861(90)85002-6.
8. Henrici-Olivé, G.; Olivé, S., The Fischer-Tropsch Synthesis: Molecular Weight Distribution of Primary Products and Reaction Mechanism. *Angew. Chem., Int. Ed.* **1976,** *15* (3), 136-141, DOI 10.1002/anie.197601361.
9. Otto, A.; Grube, T.; Schiebahn, S.; Stolten, D., Closing the loop: captured CO2 as a feedstock in the chemical industry. *Energy Environ. Sci.* **2015,** *8* (11), 3283-3297, DOI 10.1039/C5EE02591E.
10. Schulte, H. J.; Graf, B.; Xia, W.; Muhler, M., Nitrogen- and Oxygen-Functionalized Multiwalled Carbon Nanotubes Used as Support in Iron-Catalyzed, High-Temperature Fischer-Tropsch Synthesis. *ChemCatChem* **2012,** *4* (3), 350-355, DOI 10.1002/cctc.201100275.
11. Chew, L. M.; Kangvansura, P.; Ruland, H.; Schulte, H. J.; Somsen, C.; Xia, W.; Eggeler, G.; Worayingyong, A.; Muhler, M., Effect of nitrogen doping on the reducibility, activity and selectivity of carbon nanotube-supported iron catalysts applied in CO2 hydrogenation. *Appl. Catal., A* **2014,** *482*, 163-170, DOI 10.1016/j.apcata.2014.05.037.
12. Schaaf, T.; Grünig, J.; Schuster, M. R.; Rothenfluh, T.; Orth, A., Methanation of CO2 - storage of renewable energy in a gas distribution system. *Energy Sustain. Soc.* **2014,** *4* (1), 2, DOI 10.1186/s13705-014-0029-1.

13. Bui, M.; Adjiman, C. S.; Bardow, A.; Anthony, E. J.; Boston, A.; Brown, S.; Fennell, P. S.; Fuss, S.; Galindo, A.; Hackett, L. A.; Hallett, J. P.; Herzog, H. J.; Jackson, G.; Kemper, J.; Krevor, S.; Maitland, G. C.; Matuszewski, M.; Metcalfe, I. S.; Petit, C.; Puxty, G.; Reimer, J.; Reiner, D. M.; Rubin, E. S.; Scott, S. A.; Shah, N.; Smit, B.; Trusler, J. P. M.; Webley, P.; Wilcox, J.; Mac Dowell, N., Carbon capture and storage (CCS): the way forward. *Energy Environ. Sci.* **2018**, 1062-1172, DOI 10.1039/C7EE02342A.
14. Pastor-Pérez, L.; Saché, E. L.; Jones, C.; Gu, S.; Arellano-Garcia, H.; Reina, T. R., Synthetic natural gas production from CO2 over Ni-x/CeO2-ZrO2 (x = Fe, Co) catalysts: Influence of promoters and space velocity. *Catal. Today* **2018,** *317*, 108-113, DOI 10.1016/j.cattod.2017.11.035.
15. Mattia, D.; Jones, M. D.; O'Byrne, J. P.; Griffiths, O. G.; Owen, R. E.; Sackville, E.; McManus, M.; Plucinski, P., Towards Carbon-Neutral CO2 Conversion to Hydrocarbons. *ChemSusChem* **2015,** *8* (23), 4064-4072, DOI 10.1002/cssc.201500739.
16. Owen, R. E.; Mattia, D.; Plucinski, P.; Jones, M. D., Kinetics of CO2 Hydrogenation to Hydrocarbons over Iron–Silica Catalysts. *ChemPhysChem* **2017,** *18* (22), 3211-3218, DOI 10.1002/cphc.201700422.
17. Torrente-Murciano, L.; Mattia, D.; Jones, M. D.; Plucinski, P. K., Formation of hydrocarbons via CO2 hydrogenation – A thermodynamic study. *J. CO2 Util.* **2014,** *6*, 34-39, DOI 10.1016/j.jcou.2014.03.002.
18. Zhu, M.; Wachs, I. E., Iron-Based Catalysts for the High-Temperature Water–Gas Shift (HT-WGS) Reaction: A Review. *ACS Catal.* **2016,** *6* (2), 722-732, DOI 10.1021/acscatal.5b02594.
19. Yang, L.; Pastor-Pérez, L.; Gu, S.; Sepúlveda-Escribano, A.; Reina, T. R., Highly efficient Ni/CeO2-Al2O3 catalysts for CO2 upgrading via reverse water-gas shift: Effect of selected transition metal promoters. *Appl. Catal., B* **2018,** *232*, 464-471, DOI 10.1016/j.apcatb.2018.03.091.
20. Pastor-Pérez, L.; Baibars, F.; Le Sache, E.; Arellano-García, H.; Gu, S.; Reina, T. R., CO2 valorisation via Reverse Water-Gas Shift reaction using advanced Cs doped Fe-Cu/Al2O3 catalysts. *J. CO2 Util.* **2017,** *21*, 423-428, DOI 10.1016/j.jcou.2017.08.009.
21. Pham, T. H.; Qi, Y.; Yang, J.; Duan, X.; Qian, G.; Zhou, X.; Chen, D.; Yuan, W., Insights into Hägg Iron-Carbide-Catalyzed Fischer–Tropsch Synthesis: Suppression of CH4 Formation and Enhancement of C–C Coupling on χ-Fe5C2 (510). *ACS Catal.* **2015,** *5* (4), 2203-2208, DOI 10.1021/cs501668g.
22. Sirikulbodee, P.; Ratana, T.; Sornchamni, T.; Phongaksorn, M.; Tungkamani, S., Catalytic performance of Iron-based catalyst in Fischer–Tropsch synthesis using CO2 containing syngas. *Energy Procedia* **2017,** *138*, 998-1003, DOI 10.1016/j.egypro.2017.10.112.
23. Ordomsky, V. V.; Legras, B.; Cheng, K.; Paul, S.; Khodakov, A. Y., The role of carbon atoms of supported iron carbides in Fischer-Tropsch synthesis. *Catal. Sci. Technol.* **2015,** *5* (3), 1433-1437, DOI 10.1039/C4CY01631A.
24. Xu, K.; Sun, B.; Lin, J.; Wen, W.; Pei, Y.; Yan, S.; Qiao, M.; Zhang, X.; Zong, B., ε-Iron carbide as a low-temperature Fischer–Tropsch synthesis catalyst. *Nat. Commun.* **2014,** *5*, 5783, DOI 10.1038/ncomms6783.
25. Ando, H.; Matsumura, Y.; Souma, Y., A comparative study on hydrogenation of carbon dioxide and carbon monoxide over iron catalyst. *J. Mol. Catal. A: Chem.* **2000,** *154* (1), 23-29, DOI 10.1016/S1381-1169(99)00359-3.
26. Minett, D. R.; O'Byrne, J. P.; Pascu, S. I.; Plucinski, P. K.; Owen, R. E.; Jones, M. D.; Mattia, D., Fe@CNT-monoliths for the conversion of carbon dioxide to hydrocarbons: structural

characterisation and Fischer-Tropsch reactivity investigations. *Catal. Sci. Technol.* **2014,** *4* (9), 3351-3358, DOI 10.1039/C4CY00616J.
27. Serp, P.; Corrias, M.; Kalck, P., Carbon nanotubes and nanofibers in catalysis. *Appl. Catal., A* **2003,** *253* (2), 337-358, DOI 10.1016/s0926-860x(03)00549-0.
28. Galvis, H. M. T.; Bitter, J. H.; Davidian, T.; Ruitenbeek, M.; Dugulan, A. I.; de Jong, K. P., Iron Particle Size Effects for Direct Production of Lower Olefins from Synthesis Gas. *J. Am. Chem. Soc.* **2012,** *134* (39), 16207-16215, DOI 10.1021/ja304958u.
29. van Steen, E.; Prinsloo, F. F., Comparison of preparation methods for carbon nanotubes supported iron Fischer-Tropsch catalysts. *Catal. Today* **2002,** *71* (3-4), 327-334, DOI 10.1016/s0920-5861(01)00459-x.
30. Tavasoli, A.; Trepanier, M.; Abbaslou, R. M. M.; Dalai, A. K.; Abatzoglou, N., Fischer-Tropsch synthesis on mono- and bimetallic Co and Fe catalysts supported on carbon nanotubes. *Fuel Process. Technol.* **2009,** *90* (12), 1486-1494, DOI 10.1016/j.fuproc.2009.07.007.
31. Bahome, M. C.; Jewell, L. L.; Hildebrandt, D.; Glasser, D.; Coville, N. J., Fischer-Tropsch synthesis over iron catalysts supported on carbon nanotubes. *Appl. Catal., A* **2005,** *287* (1), 60-67, DOI 10.1016/j.apcata.2005.03.029.
32. Chen, W.; Fan, Z. L.; Pan, X. L.; Bao, X. H., Effect of confinement in carbon nanotubes on the activity of Fischer-Tropsch iron catalyst. *J. Am. Chem. Soc.* **2008,** *130* (29), 9414-9419, DOI 10.1021/ja8008192.
33. Abbaslou, R. M. M.; Soltan, J.; Dalai, A. K., Effects of nanotubes pore size on the catalytic performances of iron catalysts supported on carbon nanotubes for Fischer-Tropsch synthesis. *Appl. Catal., A* **2010,** *379* (1-2), 129-134, DOI 10.1016/j.apcata.2010.03.006.
34. O'Byrne, J. P.; Owen, R. E.; Minett, D. R.; Pascu, S. I.; Plucinski, P. K.; Jones, M. D.; Mattia, D., High CO2 and CO conversion to hydrocarbons using bridged Fe nanoparticles on carbon nanotubes. *Catal. Sci. Technol.* **2013,** *3* (5), 1202-1207, DOI 10.1039/C3CY20854K.
35. Daza, Y. A.; Kuhn, J. N., CO2 conversion by reverse water gas shift catalysis: comparison of catalysts, mechanisms and their consequences for CO2 conversion to liquid fuels. *RSC Adv.* **2016,** *6* (55), 49675-49691, DOI 10.1039/c6ra05414e.
36. Lu, J.; Yang, L.; Xu, B.; Wu, Q.; Zhang, D.; Yuan, S.; Zhai, Y.; Wang, X.; Fan, Y.; Hu, Z., Promotion Effects of Nitrogen Doping into Carbon Nanotubes on Supported Iron Fischer–Tropsch Catalysts for Lower Olefins. *ACS Catal.* **2014,** *4* (2), 613-621, DOI 10.1021/cs400931z.
37. Bell, T. E.; Zhan, G.; Wu, K.; Zeng, H. C.; Torrente-Murciano, L., Modification of Ammonia Decomposition Activity of Ruthenium Nanoparticles by N-Doping of CNT Supports. *Top. Catal.* **2017,** *60* (15), 1251-1259, DOI 10.1007/s11244-017-0806-0.
38. Dai, L.; Chang, D. W.; Baek, J.-B.; Lu, W., Carbon Nanomaterials for Advanced Energy Conversion and Storage. *Small* **2012,** *8* (8), 1130-1166, DOI doi:10.1002/smll.201101594.
39. Lee, W. J.; Maiti, U. N.; Lee, J. M.; Lim, J.; Han, T. H.; Kim, S. O., Nitrogen-doped carbon nanotubes and graphene composite structures for energy and catalytic applications. *Chem. Commun.* **2014,** *50* (52), 6818-6830, DOI 10.1039/C4CC00146J.
40. Xiong, H.; Motchelaho, M. A.; Moyo, M.; Jewell, L. L.; Coville, N. J., Fischer–Tropsch synthesis: Iron-based catalysts supported on nitrogen-doped carbon nanotubes synthesized by post-doping. *Appl. Catal., A* **2014,** *482*, 377-386, DOI 10.1016/j.apcata.2014.06.019.
41. Collins, P. G., Defects and Disorder in Carbon Nanotubes. In *Oxford Handbook of Nanoscience and Technology: Materials*, Oxford University Press: Oxford, 2009; Vol. 2, pp 31-93.

42. Mattia, D.; Williamson, D.; Jones, M. D., Highly selective, iron-driven CO2 methanation. *Energ. Technol. 0* (ja), DOI 10.1002/ente.201800923.
43. Sharifi, T.; Nitze, F.; Barzegar, H. R.; Tai, C.-W.; Mazurkiewicz, M.; Malolepszy, A.; Stobinski, L.; Wågberg, T., Nitrogen doped multi walled carbon nanotubes produced by CVD-correlating XPS and Raman spectroscopy for the study of nitrogen inclusion. *Carbon* **2012,** *50* (10), 3535-3541, DOI 10.1016/j.carbon.2012.03.022.
44. Dresselhaus, M. S.; Jorio, A.; Souza Filho, A. G.; Saito, R., Defect characterization in graphene and carbon nanotubes using Raman spectroscopy. *Philos. Trans. Royal Soc. A* **2010,** *368* (1932), 5355, DOI 10.1098/rsta.2010.0213.
45. Yadav, R. M.; Srivastava, A.; Srivastava, O. N., Synthesis of Bamboo-Shaped Carbon-Nitrogen Nanotubes Using Acetonitrile-Ferrocene Precursor. *J. Nanosci. Nanotechnol.* **2004,** *4* (7), 719-721, DOI 10.1166/jnn.2004.105.
46. Yadav, R. M.; Shripathi, T.; Srivastava, A.; Srivastava, O. N., Effect of Ferrocene Concentration on the Synthesis of Bamboo-Shaped Carbon & Nitrogen Nanotube Bundles. *J. Nanosci. Nanotechnol.* **2005,** *5* (5), 820-824, DOI 10.1166/jnn.2005.102.
47. Yadav, R.; Dobal, P.; Shripathi, T.; Katiyar, R.; Srivastava, O., Effect of Growth Temperature on Bamboo-shaped Carbon–Nitrogen (C–N) Nanotubes Synthesized Using Ferrocene Acetonitrile Precursor. *Nanoscale Res. Lett.* **2008,** *4* (3), 197, DOI 10.1007/s11671-008-9225-2.
48. Maldonado, S.; Morin, S.; Stevenson, K. J., Structure, composition, and chemical reactivity of carbon nanotubes by selective nitrogen doping. *Carbon* **2006,** *44* (8), 1429-1437, DOI 10.1016/j.carbon.2005.11.027.
49. DiLeo, R. A.; Landi, B. J.; Raffaelle, R. P., Purity assessment of multiwalled carbon nanotubes by Raman spectroscopy. *J. Appl. Phys.* **2007,** *101* (6), 5, DOI 10.1063/1.2712152.
50. Kim, K. K.; Park, J. S.; Kim, S. J.; Geng, H. Z.; An, K. H.; Yang, C.-M.; Sato, K.; Saito, R.; Lee, Y. H., Dependence of Raman spectra G' band intensity on metallicity of single-wall carbon nanotubes. *Phys. Rev. B* **2007,** *76* (20), 205426, DOI 10.1103/PhysRevB.76.205426.
51. Webster, S.; Maultzsch, J.; Thomsen, C.; Liu, J.; Czerw, R.; Terrones, M.; Adar, F.; John, C.; Whitley, A.; Carroll, D. L., Raman Characterization of Nitrogen Doped Multiwalled Carbon Nanotubes. *Mater. Res. Soc. Symp. Proc.* **2003,** *772*, M7.8, DOI 10.1557/PROC-772-M7.8.
52. Torres Galvis, H. M.; Bitter, J. H.; Davidian, T.; Ruitenbeek, M.; Dugulan, A. I.; de Jong, K. P., Iron Particle Size Effects for Direct Production of Lower Olefins from Synthesis Gas. *J. Am. Chem. Soc.* **2012,** *134* (39), 16207-16215, DOI 10.1021/ja304958u.
53. Yin-Chih, L.; Jhen-Yong, H.; Chia-Nan, Y.; Shi-Yuan, T.; Mean-Jue, T.; Hung-Wei, S.; Chia-Hao, C.; Minn-Tsong, L., X-ray photoelectron spectroscopic investigation on Fe geometrical sites of iron nitride thin films. *Jpn. J. Appl. Phys* **2015,** *54* (3), 033002, DOI 10.7567/JJAP.54.033002.
54. Yamashita, T.; Hayes, P., Analysis of XPS spectra of Fe2+ and Fe3+ ions in oxide materials. *Appl. Surf. Sci.* **2008,** *254* (8), 2441-2449, DOI 10.1016/j.apsusc.2007.09.063.
55. Biesinger, M. C.; Payne, B. P.; Grosvenor, A. P.; Lau, L. W. M.; Gerson, A. R.; Smart, R. S. C., Resolving surface chemical states in XPS analysis of first row transition metals, oxides and hydroxides: Cr, Mn, Fe, Co and Ni. *Appl. Surf. Sci.* **2011,** *257* (7), 2717-2730, DOI 10.1016/j.apsusc.2010.10.051.
56. Ewels, C.; Glerup, M., Nitrogen doping in carbon nanotubes. *J. Nanosci. Nanotechnol.* **2005,** *5* (9), 1345-1363, DOI 10.1166/jnn.2005.304.

57. Chen, D.; Tang, Q.; Li, X.; Zhou, X.; Zang, J.; Xue, W.-q.; Xiang, J.-y.; Guo, C.-q., Biocompatibility of magnetic Fe(3)O(4) nanoparticles and their cytotoxic effect on MCF-7 cells. *Int. J. Nanomedicine* **2012,** *7*, 4973-4982, DOI 10.2147/IJN.S35140.
58. Azam, A.; Ahmed, A. S.; Oves, M.; Khan, M. S.; Habib, S. S.; Memic, A., Antimicrobial activity of metal oxide nanoparticles against Gram-positive and Gram-negative bacteria: a comparative study. *Int. J. Nanomedicine* **2012,** *7*, 6003-6009, DOI 10.2147/IJN.S35347.
59. Abatzoglou, N.; Legras, B., Nano-iron carbide-catalyzed Fischer-Tropsch synthesis of green fuel: surface reaction kinetics-controlled regimes in a 3-φ slurry-continuous stirred tank reactor. *IJEPR* **2015,** *3* (1), 9-15, DOI 10.11159/ijepr.2015.002.
60. Li, Y.; Hu, Y.; Huang, G.; Li, C., Metallic iron nanoparticles: Flame synthesis, characterization and magnetic properties. *Particuology* **2013,** *11* (4), 460-467, DOI 10.1016/j.partic.2012.10.008.
61. Gong, K.; Du, F.; Xia, Z.; Durstock, M.; Dai, L., Nitrogen-Doped Carbon Nanotube Arrays with High Electrocatalytic Activity for Oxygen Reduction. *Science* **2009,** *323* (5915), 760, DOI 10.1126/science.1168049.
62. Geng, D.; Chen, Y.; Chen, Y.; Li, Y.; Li, R.; Sun, X.; Ye, S.; Knights, S., High oxygen-reduction activity and durability of nitrogen-doped graphene. *Energy Environ. Sci.* **2011,** *4* (3), 760-764, DOI 10.1039/C0EE00326C.

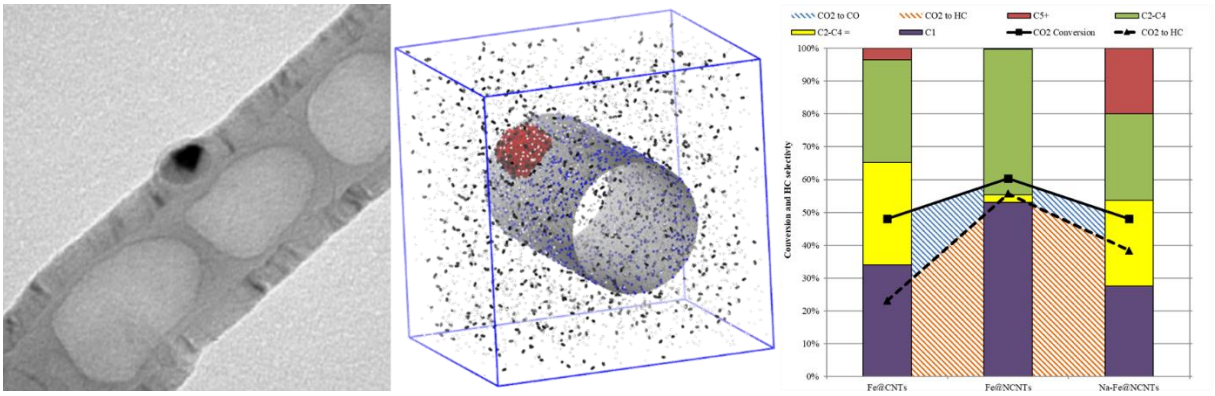

C—N dipoles in a CO_2 hydrogenation catalyst result in increased reactant attraction, conversion, and a significant shift in products.